

Chaotic shadow of a non-Kerr rotating compact object with quadrupole mass moment

Mingzhi Wang,¹ Songbai Chen,^{1,2,3,4,*} and Jiliang Jing^{1,2,3,4,†}

¹*Institute of Physics and Department of Physics, Hunan Normal University, Changsha, Hunan 410081, People's Republic of China*

²*Key Laboratory of Low Dimensional Quantum Structures and Quantum Control of Ministry of Education, Hunan Normal University, Changsha, Hunan 410081, People's Republic of China*

³*Synergetic Innovation Center for Quantum Effects and Applications, Hunan Normal University, Changsha, Hunan 410081, People's Republic of China*

⁴*Center for Gravitation and Cosmology, College of Physical Science and Technology, Yangzhou University, Yangzhou 225009, People's Republic of China*



(Received 12 March 2018; published 26 November 2018)

We have studied numerically the shadows of a non-Kerr rotating compact object with a quadrupole mass moment, which belongs to the Manko-Novikov family. The nonintegrable photon motion caused by a quadrupole mass moment sharply affects the shadow of the compact object. As the deviation parameter related to the quadrupole mass moment is negative, the shadow of the compact object is prolate, and there are two disconnected main shadows with eyebrows located symmetrically on both sides of the equatorial plane. As the deviation parameter is positive, the shadow becomes oblate, and the main shadow is joined together in the equatorial plane. Moreover, in these positive cases, there is a disorder region in the left of the shadow that increases with the quadrupole-deviation parameter. Interestingly, we also find that the Einstein ring is broken as the deviation from the Kerr metric is larger than a certain critical value. This critical value decreases with the rotation parameter of the black hole. Especially, the observer on the direction of the rotation axis will find some concentric bright rings in the black disk. Finally, supposing that the gravitational field of the supermassive central object of the galaxy is described by this metric, we estimate the numerical values of the observables for the black hole shadow.

DOI: 10.1103/PhysRevD.98.104040

I. INTRODUCTION

The current observations of gravitational waves [1–5] confirm the existence of black holes in our Universe. According to the no-hair theorem [6], one can find that a neutral rotating black hole in asymptotically flat and matter-free spacetime is described entirely by the Kerr metric, which is characterized uniquely by a mass and an angular momentum, and then all rotating astrophysical black holes in our Universe should be Kerr black holes. However, there is no direct evidence to indicate that black hole candidates must be Kerr black holes, even if the current observations of gravitational waves [1–5] cannot exclude the possibility that the geometry of these candidates significantly deviates from the Kerr metric. Therefore, studying in detail the properties of a generic non-Kerr rotating black hole and the corresponding observable effects becomes very significant [7–9] since they can help us to understand features of a black hole and to further examine the no-hair theorem.

One of the important non-Kerr rotating asymptotically flat spacetimes is Manko-Novikov spacetime [10], which is an exact stationary and axial symmetric solution of the vacuum Einstein equations. Generally, besides the mass and rotation parameters, Manko-Novikov spacetime also possesses an infinite number of free parameters related to multipole moments, which describe the deviations away from the Kerr metric. Here, we focus on only a particular subclass of the Manko-Novikov metric with a single deviation parameter denoting the difference from the Kerr case at the mass quadrupole order [11]. Although there exist the naked singularity and the closed timelike curves, such a Manko-Novikov spacetime is still a good test bed for exploring various observable consequences of deviations from the Kerr metric since the nonintegrable particle motion originating from the quadrupole-deviation parameter does not appear in the Kerr black hole spacetime [10–13], and the corresponding observable properties of nonintegrable orbits could help us to further test the Kerr black hole hypothesis.

The black hole shadow is a two-dimensional dark region in the observer's sky corresponding to light rays that fall into an event horizon when propagated backward in time. It is well known that the shape and size of the shadow carry

*csb3752@hunnu.edu.cn

†jljing@hunnu.edu.cn

the fingerprint of the geometry around the black hole [14–16] and then the shadow can be regarded as a potential tool to probe black hole parameters in the future observation, such as Event Horizon Telescope [17,18] and European Black Hole Cam [19]. The shadow of a Schwarzschild black hole is a perfect black disk, but for a rotating black hole, it becomes an elongated silhouette due to the so-called dragging effect [15,16]. The cusp silhouette of the shadow emerges in the spacetime of a Kerr black hole with Proca hair [20] and of a Konoplya-Zhidenko rotating non-Kerr black hole [21] as the suitable spacetime parameters are selected. Especially, the self-similar fractal structures are found in the black hole shadow for the cases in which the photon motion is not variable separable, such as a Kerr black hole with scalar hair [22–25], a binary black hole system [26,27], or Bonnor black diholes with a magnetic dipole moment [28]. The recent investigation indicates that these novel structure and patterns in shadows are determined actually by the nonplanar bound photon orbits [20] and the invariant phase space structures [29] for the photon motion in the background spacetimes. Moreover, the shadows of black holes characterized by other parameters have been studied recently [30–49] and indicate that these parameters give rise to the richer silhouettes for black hole shadows in various theories of gravity.

In this paper, we will study the shadow of a non-Kerr rotating compact object with a quadrupole mass moment [10–12], which is Manko-Novikov spacetime with a single quadrupole-deviation parameter. Since the presence of the deviation parameter could lead to the chaotic motion of a photon, it is expected that the pattern and structures of the shadow will have some essential features different from that of a Kerr black hole. The main purpose of this paper is to probe the new features of the shadow casted by the non-Kerr rotating compact object with a quadrupole mass moment [10–12] and to detect the effect of quadrupole-deviation parameter on the shadow.

The paper is organized as follows. In Sec. II, we review briefly the Manko-Novikov metric and then analyze equation of photon motion in this spacetime. In Sec. III, with the backward ray-tracing method, we numerically present the shadows for the non-Kerr rotating compact object with a quadrupole mass moment and probe the effect of the quadrupole-deviation parameter on the shadow for the compact object. In Sec. IV, we suppose that the gravitational field of the supermassive black hole at the center of our Galaxy can be described by the spacetime of a non-Kerr rotating black hole with a quadrupole mass moment and then obtain the numerical results for the observables about the black hole shadow. Finally, we present a summary.

II. MANKO-NOVIKOV SPACETIME AND NULL GEODESICS

The Manko-Novikov metric is an exact stationary, axial symmetric solution of the vacuum Einstein equations with

extra higher-order moments that describe the deviations away from the Kerr metric [10–12]. Generally, the Manko-Novikov solution has an infinite number of free parameters, and the presence of these parameters could destroy the event horizon, which implies that it is not a black hole spacetime within a certain range of parameters. Here, we focus on only a particular subclass of the Manko-Novikov metric that depends on three parameters: the mass M , the spin S , and the dimensionless parameter q . The first two parameters are identical to those of the corresponding Kerr metric, but the third parameter q measures the deviation of Manko-Novikov quadrupole mass moment Q from the Kerr quadrupole moment $Q_{\text{Kerr}} = -S^2/M$, i.e., $q = -(Q - Q_{\text{Kerr}})/M^3$. In the prolate spheroidal coordinates, this Manko-Novikov metric can be described by a Weyl-Papapetrou line element as [10–13,50]

$$ds^2 = -f(dt - \omega d\phi)^2 + k^2 f^{-1} e^{2\gamma} (x^2 - y^2) \left(\frac{dx^2}{x^2 - 1} + \frac{dy^2}{1 - y^2} \right) + k^2 f^{-1} (x^2 - 1)(1 - y^2) d\phi^2, \quad (1)$$

where

$$\alpha = \frac{-M + \sqrt{M^2 - (S/M)^2}}{(S/M)}, \quad (2)$$

$$k = M \frac{1 - \alpha^2}{1 + \alpha^2}, \quad (3)$$

$$\beta = q \frac{M^3}{k^3}, \quad (4)$$

$$f = e^{2\psi} \frac{A}{B}, \quad (5)$$

$$\omega = 2ke^{-2\psi} \frac{C}{A} - 4k \frac{\alpha}{1 - \alpha^2}, \quad (6)$$

$$e^{2\gamma} = e^{2\gamma'} \frac{A}{(x^2 - 1)(1 - \alpha^2)^2}, \quad (7)$$

$$A = (x^2 - 1)(1 + ab)^2 - (1 - y^2)(b - a)^2, \quad (8)$$

$$B = [(x + 1) + (x - 1)ab]^2 + [(1 + y)a + (1 - y)b]^2, \quad (9)$$

$$C = (x^2 - 1)(1 + ab)[(b - a) - y(a + b)] + (1 - y^2)(b - a)[(1 + ab) + x(1 - ab)], \quad (10)$$

$$\psi = \beta \frac{P_2}{R^3}, \quad (11)$$

$$\gamma' = \ln \sqrt{\frac{x^2 - 1}{x^2 - y^2}} + \frac{3\beta^2}{2R^6} (P_3^2 - P_2^2) + \beta \left(-2 + \sum_{\ell=0}^2 \frac{x - y + (-1)^{2-\ell}(x+y)P_\ell}{R^{\ell+1}} \right), \quad (12)$$

$$a = -\alpha \exp \left[-2\beta \left(-1 + \sum_{\ell=0}^2 \frac{(x-y)P_\ell}{R^{\ell+1}} \right) \right], \quad (13)$$

$$b = \alpha \exp \left[2\beta \left(1 + \sum_{\ell=0}^2 \frac{(-1)^{3-\ell}(x+y)P_\ell}{R^{\ell+1}} \right) \right], \quad (14)$$

$$R = \sqrt{x^2 + y^2 - 1}, \quad (15)$$

$$P_\ell = P_\ell \left(\frac{xy}{R} \right), \quad (16)$$

and $P_\ell(z)$ are the l -order Legendre polynomials. The parameter $q > 0$ represents an oblate deviation of the Kerr metric, while $q < 0$ represents a prolate deviation. As q vanishes, the Manko-Novikov metric (1) reduces exactly to the Kerr metric. Another spacetime metric describing the gravitational field of a compact object with a quadrupole mass moment is the so-called quasi-Kerr metric [51], which is obtained by perturbing the Kerr metric with the help of the well-known Hartle-Thorne exterior metric [52]. This quasi-Kerr metric is fully accurate up to the first order in terms of the dimensionless quadrupole moment parameter q and the second order in terms of the angular momentum. Although the quasi-Kerr metric can be reduced to Kerr case as the parameter q disappears, it is valid only on the slowly rotating cases. This is different from the Manko-Novikov metric in which there is no such restriction on the rotation parameter.

With a coordinate change [10–13,50,53,54],

$$x = \frac{r - M}{k}, \quad y = \cos \theta, \quad (17)$$

the Manko-Novikov metric (1) can be rewritten as a form in the standard Boyer-Lindquist coordinates

$$ds^2 = -f(dt - \omega d\phi)^2 + \frac{e^{2\gamma}\rho^2}{f\Delta} dr^2 + \frac{e^{2\gamma}\rho^2}{f} d\theta^2 + \frac{\Delta \sin^2 \theta}{f} d\phi^2, \quad (18)$$

where $\rho^2 = (r - M)^2 - k^2 \cos^2 \theta$, $\Delta = (r - M)^2 - k^2$. And then the outer event horizon radius is $r_h = M + k$. The Hamiltonian of a photon motion along the null geodesic in the spacetime (18) can be expressed as

$$\mathcal{H}(x, p) = \frac{1}{2} g^{\mu\nu}(x) p_\mu p_\nu = \frac{1}{2} \left[\left(-\frac{1}{f} + \frac{f\omega^2}{\Delta \sin^2 \theta} \right) p_t^2 + \frac{f\Delta}{e^{2\gamma}\rho^2} p_r^2 + \frac{f}{e^{2\gamma}\rho^2} p_\theta^2 + \frac{f}{\Delta \sin^2 \theta} p_\phi^2 + 2 \frac{f\omega}{\Delta \sin^2 \theta} p_t p_\phi \right] = 0, \quad (19)$$

where p_r and p_θ are the components of momentum of the photon $p_r = g_{rr}\dot{r}$ and $p_\theta = g_{\theta\theta}\dot{\theta}$. Obviously, t and ϕ are two cyclic coordinates for the spacetime (18) since the metric functions are independent of these two coordinates. Therefore, there exist two conserved quantities E and L for the motion of photon, i.e.,

$$E = -p_t = f\dot{t} - f\omega\dot{\phi}, \quad L = p_\phi = f\omega\dot{t} + \left(\frac{\Delta \sin^2 \theta}{f} - f\omega^2 \right) \dot{\phi}, \quad (20)$$

which correspond to the energy and the z component of the angular momentum of a photon moving in the spacetime, respectively. With these two conserved quantities, we can find the null geodesic equations of the photon can be expressed as

$$\dot{t} = \frac{E}{f} + \frac{f\omega(L - E\omega)}{\Delta \sin^2 \theta}, \quad (21)$$

$$\begin{aligned} \ddot{r} = & \frac{1}{2} \frac{\partial}{\partial r} \left[\ln \left(\frac{f\Delta}{e^{2\gamma}\rho^2} \right) \right] \dot{r}^2 + \frac{\partial}{\partial \theta} \left[\ln \left(\frac{f}{e^{2\gamma}\rho^2} \right) \right] \dot{r} \dot{\theta} \\ & + \frac{\Delta}{2} \frac{\partial}{\partial r} \left[\ln \left(\frac{e^{2\gamma}\rho^2}{f} \right) \right] \dot{\theta}^2 - \frac{E^2 \Delta f_{,r}}{2f e^{2\gamma}\rho^2} \\ & + \frac{f(L - E\omega)[2Ef\Delta\omega_{,r} + (L - E\omega)(f\Delta_{,r} - f_{,r}\Delta)]}{2e^{2\gamma}\rho^2 \Delta \sin^2 \theta}, \end{aligned} \quad (22)$$

$$\begin{aligned} \ddot{\theta} = & \frac{1}{2\Delta} \frac{\partial}{\partial \theta} \left[\ln \left(\frac{e^{2\gamma}\rho^2}{f} \right) \right] \dot{r}^2 + \frac{\partial}{\partial r} \left[\ln \left(\frac{f}{e^{2\gamma}\rho^2} \right) \right] \dot{r} \dot{\theta} \\ & + \frac{1}{2} \frac{\partial}{\partial \theta} \left[\ln \left(\frac{f}{e^{2\gamma}\rho^2} \right) \right] \dot{\theta}^2 - \frac{f(L - E\omega)^2 f_{,\theta}}{2e^{2\gamma}\rho^2 \Delta \sin^2 \theta} \\ & - \frac{E^2 f_{,\theta}}{2f e^{2\gamma}\rho^2} + \frac{f(L - E\omega)[(L - E\omega)\cot \theta + E\omega_{,\theta}]}{e^{2\gamma}\rho^2 \Delta \sin^2 \theta}, \end{aligned} \quad (23)$$

$$\dot{\phi} = \frac{f(L - E\omega)}{\Delta \sin^2 \theta}, \quad (24)$$

with the constraint condition

$$H \equiv e^{2\gamma}\rho^2[\dot{r}^2 + \Delta\dot{\theta}^2] - E^2\Delta + \frac{f^2}{\sin^2 \theta}(L - \omega E)^2 = 0. \quad (25)$$

Obviously, the presence of quadrupole-deviation parameter q yields that the null geodesics equations are not be variable separable because there is no existence of Carter-like constant in the Manko-Novikov spacetime (18) and then only two integrals of motion E and L are admitted in this case. This implies that the motion of the photon could be chaotic, which should affect the shadow of a non-Kerr rotating compact object with a quadrupole mass moment (18).

III. SHADOW CAST BY A NON-KERR ROTATING COMPACT OBJECT WITH QUADRUPOLE MASS MOMENT

Let us now study the shadows cast by a non-Kerr rotating compact object with a quadrupole mass moment with the “backward ray-tracing” method [22–30]. In this method, the light rays are assumed to evolve from the observer backward in time, and the information carried by each ray would be assigned to a pixel in a final image in the observer’s sky. With this spirit, we solve numerically the null geodesic equations (20) and (21) for each pixel in the final image with the corresponding initial condition and obtain the image of the shadow in observer’s sky, which is composed of the pixels connected to the light rays falling down into the horizon of the black hole. Considering that the spacetime of a non-Kerr rotating compact object with a quadrupole mass moment (18) is asymptotically flat, as in Refs. [22–30], one can expand the observer basis $\{e_{\hat{t}}, e_{\hat{r}}, e_{\hat{\theta}}, e_{\hat{\phi}}\}$ as a form in the coordinate basis $\{\partial_t, \partial_r, \partial_\theta, \partial_\phi\}$,

$$e_{\hat{\mu}} = e_{\hat{\mu}}^\nu \partial_\nu, \quad (26)$$

where the transform matrix $e_{\hat{\mu}}^\nu$ obeys $g_{\mu\nu} e_{\hat{\alpha}}^\mu e_{\hat{\beta}}^\nu = \eta_{\hat{\alpha}\hat{\beta}}$ and $\eta_{\hat{\alpha}\hat{\beta}}$ is the metric of Minkowski spacetime. In general, it is not unique for the transformation (26) which satisfies both the spatial rotations and Lorentz boosts. For the Manko-Novikov spacetime (18), it is convenient to choose a decomposition associated with a reference frame with zero axial angular momentum in relation to spatial infinity [22–30,55],

$$e_{\hat{\mu}}^\nu = \begin{pmatrix} \zeta & 0 & 0 & \gamma \\ 0 & A^r & 0 & 0 \\ 0 & 0 & A^\theta & 0 \\ 0 & 0 & 0 & A^\phi \end{pmatrix}, \quad (27)$$

where $\zeta, \gamma, A^r, A^\theta$, and A^ϕ are real coefficients. From the Minkowski normalization

$$e_{\hat{\mu}} e^{\hat{\nu}} = \delta_{\hat{\mu}}^{\hat{\nu}}, \quad (28)$$

one can obtain

$$\begin{aligned} A^r &= \frac{1}{\sqrt{g_{rr}}}, & A^\theta &= \frac{1}{\sqrt{g_{\theta\theta}}}, & A^\phi &= \frac{1}{\sqrt{g_{\phi\phi}}}, \\ \zeta &= \sqrt{\frac{g_{\phi\phi}}{g_{tt}^2 - g_{tt}g_{\phi\phi}}}, & \gamma &= -\frac{g_{t\phi}}{g_{\phi\phi}} \sqrt{\frac{g_{\phi\phi}}{g_{tt}^2 - g_{tt}g_{\phi\phi}}}. \end{aligned} \quad (29)$$

Therefore, one can get the locally measured four-momentum $p^{\hat{\mu}}$ of a photon by the projection of its four-momentum p^μ onto $e_{\hat{\mu}}$,

$$p^{\hat{t}} = -p_{\hat{t}} = -e_{\hat{t}}^\nu p_\nu, \quad p^{\hat{r}} = p_{\hat{r}} = e_{\hat{r}}^\nu p_\nu. \quad (30)$$

With the help of Eq. (29), the locally measured four-momentum $p^{\hat{\mu}}$ can be further written as

$$\begin{aligned} p^{\hat{t}} &= \zeta E - \gamma L, & p^{\hat{r}} &= \frac{1}{\sqrt{g_{rr}}} p_r, \\ p^{\hat{\theta}} &= \frac{1}{\sqrt{g_{\theta\theta}}} p_\theta, & p^{\hat{\phi}} &= \frac{1}{\sqrt{g_{\phi\phi}}} L. \end{aligned} \quad (31)$$

Repeating operations similar to those in Refs. [22–30], one can obtain the position of the photon’s image in the observer’s sky,

$$\begin{aligned} x &= -r_{\text{obs}} \frac{p^{\hat{\phi}}}{p^{\hat{r}}} = -r_{\text{obs}} \frac{L}{\sqrt{e^{2\gamma} \rho^2 \left(\frac{\sin^2 \theta}{f^2} - \frac{\omega^2}{\Delta}\right) \dot{r}}}, \\ y &= r_{\text{obs}} \frac{p^{\hat{\theta}}}{p^{\hat{r}}} = r_{\text{obs}} \frac{\sqrt{\Delta} \dot{\theta}}{\dot{r}}, \end{aligned} \quad (32)$$

where the spatial position of the observer is set to $(r_{\text{obs}}, \theta_{\text{obs}})$.

To control the error in the numerical calculation of solving the coupled and complicated differential equations (21)–(24), we adopt to the corrected fifth-order Runge-Kutta method [56,57] in which the velocities $(\dot{r}, \dot{\theta})$ are corrected in integration and the numerical deviation is pulled back in a least-squares shortest path. This high-precision method has been applied extensively to study chaotic motion in various dynamical systems [56–58]. The energy of the dynamical system (21) is subjected to the constraint $H = 0$, and then H can be regarded as a conserved quantity. To ensure the high precision of the conserved quantity H in the system of Eqs. (21)–(25) at every integration, one can introduce a dimensionless parameter ξ to make a connection between the numerical velocities $(\dot{r}, \dot{\theta})$ and the true value $(\dot{r}^*, \dot{\theta}^*)$ in the form of

$$\dot{r}^* = \xi \dot{r}, \quad \dot{\theta}^* = \xi \dot{\theta}. \quad (33)$$

Inserting Eq. (33) into Eq. (25), one can find that the scale factor of velocity correction ξ in the non-Kerr rotating compact object with a quadrupole mass moment (18) has the form

$$\xi = \sqrt{\frac{E^2 \Delta - \frac{f^2}{\sin^2 \theta} (L - \omega E)^2}{e^{2\gamma} \rho^2 [\dot{r}^2 + \Delta \dot{\theta}^2]}}. \quad (34)$$

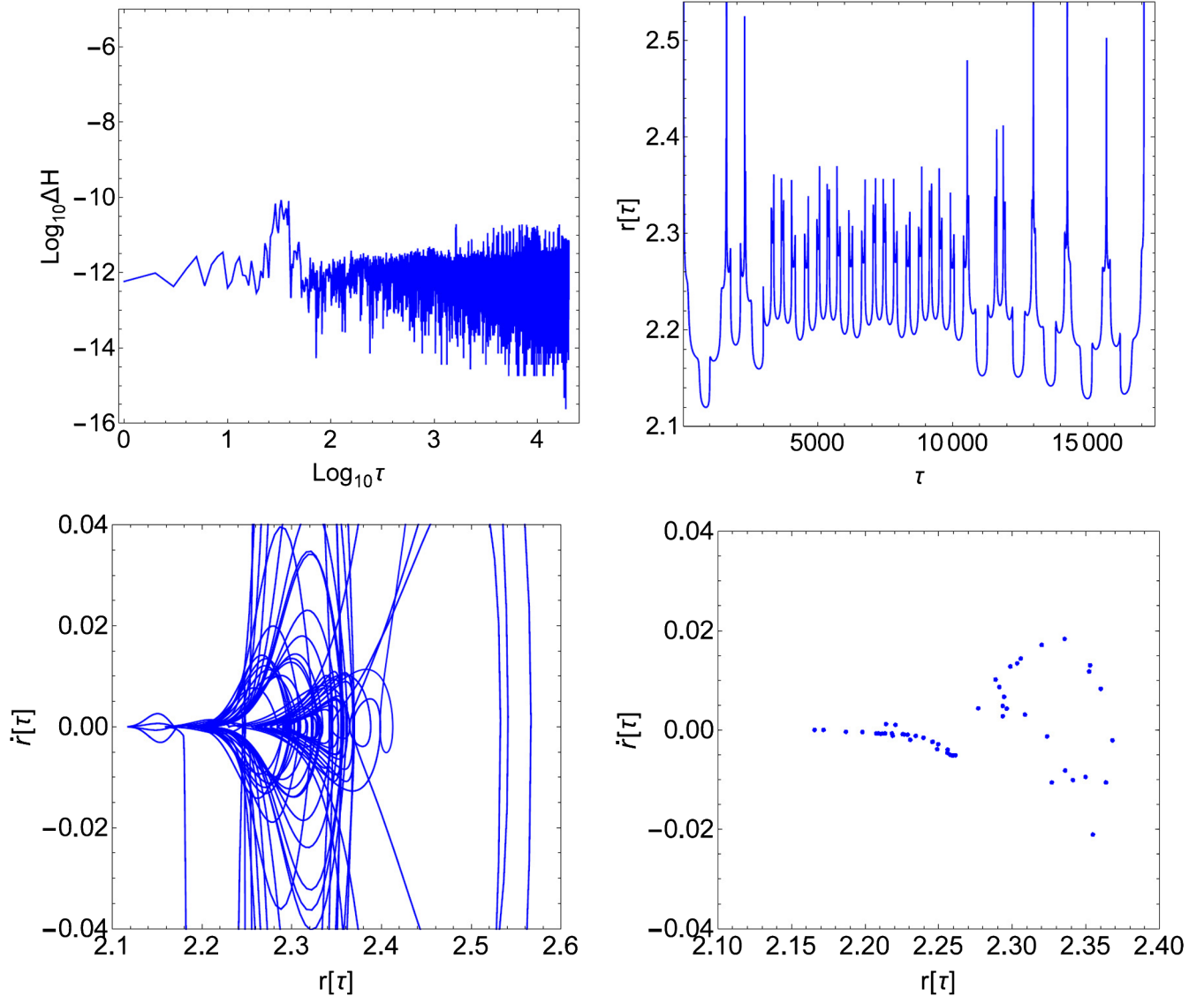


FIG. 1. The error is controlled better than 10^{-10} by the velocity correction method (RK5+Correction) for a chaotic orbit of the photon in the spacetime of a non-Kerr rotating compact object with quadrupole-deviation parameter $q = 8$ and spin parameter $S = 0.98$. The left and right panels in the top row correspond to the change of the error H and the polar coordinate r with time τ , respectively. The panels in the bottom row are the phase curve and Poincaré sections with $\theta = 2.2$ on the plane (r, \dot{r}) for the corresponding chaotic orbit of photon, respectively. Here, we set the parameters $M = 1$, $E = 1$, $L = 1.98341$ and the initial conditions $\{r(0) = 30; \dot{r}(0) = 0.987395; \theta = \pi/2\}$.

In this way, the conserved quantity H in the system of Eqs. (21)–(25) can hold perfectly at every integration. Figure 1 shows that the value of H remains below 10^{-10} , and then the error is controlled greatly, even for a chaotic orbit of the photon, which ensures that this method is powerful enough to avoid the pseudochaos caused by numerical errors.

In Figs. 2 and 3, we present the shadow of a non-Kerr rotating compact object (18) with a different quadrupole-deviation parameter q for the fixed spin parameter $S = 0.2M^2$ and $S = 0.98M^2$, respectively. Here, we set $M = 1$, and the observer is set at $r_{\text{obs}} = 30M$ with the inclination angle $\theta_{\text{obs}} = 90^\circ$. From Fig. 2, we can find that the shadow

of black hole is similar to a black disk in the case $q = 0$ as discussed in Refs. [15,16]. However, the presence of quadrupole-deviation parameter q sharply changes the shape and pattern of the shadow of the non-Kerr rotating compact object. Let us now first focus on the case with negative q . As $q = -0.5$, the shadow of the non-Kerr rotating compact object with a quadrupole mass moment becomes prolate, and it is split into two disconnected semicircular main shadows with eyebrows, which lie at symmetric positions above and below the equatorial plane. There exists an irregular bright region in each main shadow. Actually, we can detect many other smaller shadows with a self-similar fractal structure, which is caused by chaotic

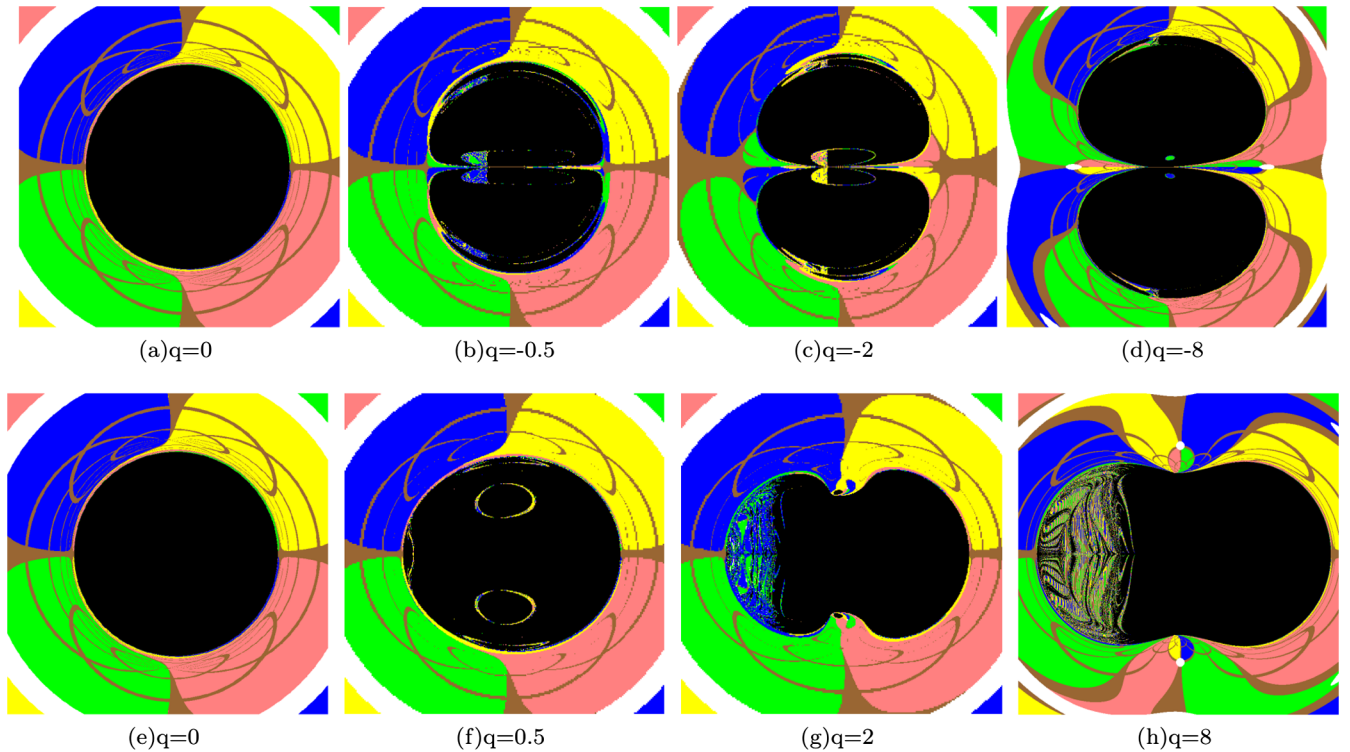


FIG. 2. The shadow of a non-Kerr rotating compact object with different quadrupole-deviation parameter q for fixed spin parameter $S = 0.2M^2$. Here, we set $M = 1$, and the observer is set at $r_{\text{obs}} = 30M$ with the inclination angle $\theta_0 = 90^\circ$.

lensing. As the deviation from the Kerr black hole becomes larger, the curvature of the boundary line near the equatorial plane increases for the main shadow, and the irregular bright regions become smaller and move right. For the case with positive q , we find that the shadow of the non-Kerr rotating compact object with a quadrupole mass moment becomes oblate and the main shadows are joined together in the equatorial plane. As $q = 0.5$, we find that two ringlike bright zones imbed symmetrically in the middle of the black shadow and an arclike bright zone appears in the left of the shadow. Moreover, there exist the eyebrowlike shadows in the region near the north and south poles. With the increase of the deviation, the shadow becomes oblate so that it turns into the shape of dumbbell for the larger q . In addition, the left black region with the arclike bright zone becomes a disorder region in which the black spots distribute dispersively, and this disorder region increases with the quadrupole-deviation parameter q . These features of the shadow mean that the shape and pattern of the shadow of a black hole with the positive q are qualitatively different from those with negative q .

In Fig. 3, we present the shadow of a rapidly rotating non-Kerr compact object with a quadrupole mass moment (18). As $q = 0$, the shadow has a D-type shape, as expected since the metric (18) is actually a rapidly rotating Kerr metric in this case. Comparing with the slowly rotating case, the shadow of a rapidly rotating non-Kerr compact object with a quadrupole mass moment has some new

features. As $q = -0.5$, there are several bright curves that split the shadow into three main parts: two eyeball-like shadows, eyebrowlike shadows, and intermediate black regions. With the increase of the deviation, we find that the two eyeball-like shadows increase, but the eyebrowlike shadows and intermediate black regions decrease so that the shadow becomes a 3-type shape as $q = -8$. For the case with positive q , there also exist two eyeball-like shadows imbedded in the main shadow with some smaller eyebrows. However, with the increase of quadrupole-deviation parameter q , the eyeball-like shadows become small, and the main shadow first decreases and then increases. The disorder region in the left of the shadow increases with the quadrupole-deviation parameter q , which is similar to that in the cases with the spin parameter $S = 0.2M^2$. In addition, from the subfigures (a), (d), (e), and (h) in Fig. 4, we find that the Einstein ring (white ring in the figures) is broken for the larger absolute value of q . The critical value of q accounting for a broken Einstein ring is listed in Table I, which shows that the absolute value $|q_c|$ decreases with the rotation parameter of the non-Kerr rotating black hole.

In Figs. 5 and 6, we also present the dependence of the shadow on the observer's inclination angle θ_{obs} with the absolute value $|q| = 2$ for $S = 0.2M^2$ and $S = 0.98M^2$, respectively. It is obvious that the shadow is center symmetric as $\theta_{\text{obs}} = 0^\circ$. With the increase of the inclination angle θ_{obs} , the center symmetry of the shadow is gradually

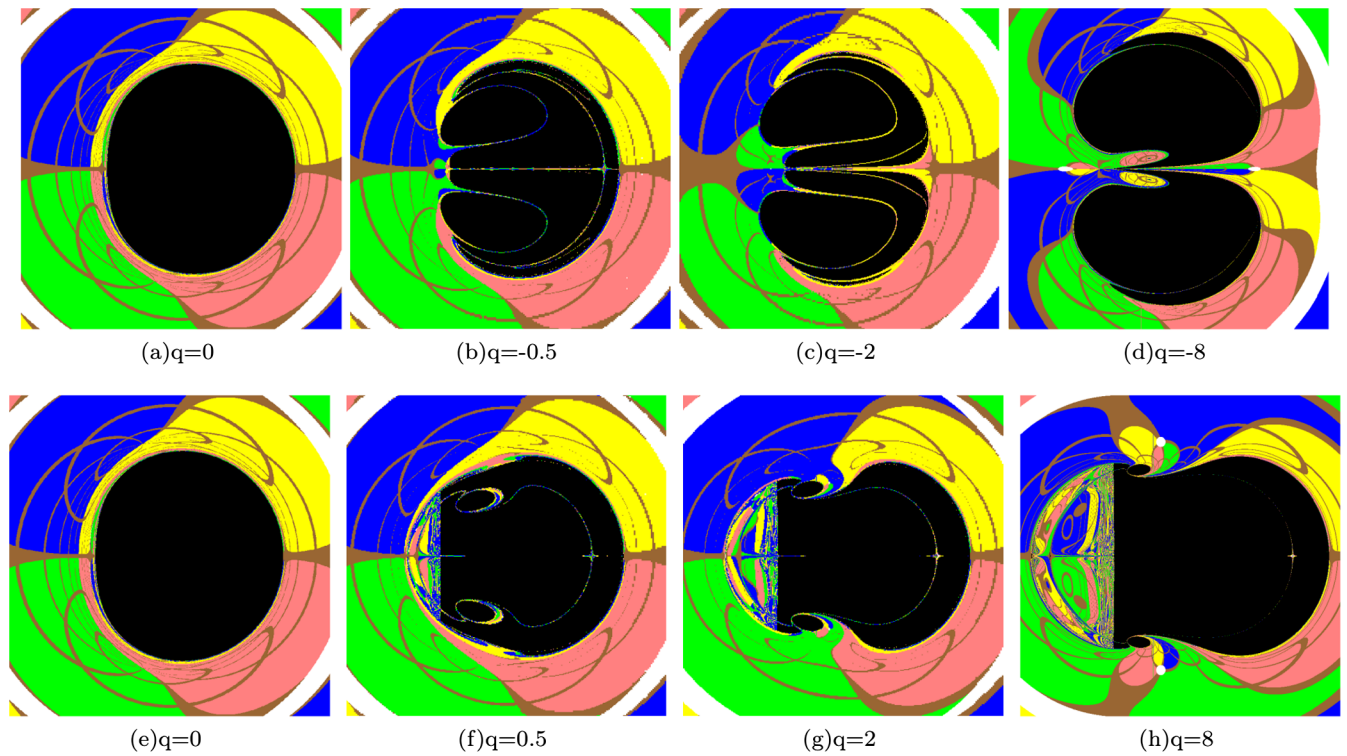


FIG. 3. The shadow of a non-Kerr rotating compact object with quadrupole-deviation parameter q for fixed spin parameter $S = 0.98M^2$. Here, we set $M = 1$, and the observer is set at $r_{\text{obs}} = 30M$ with the inclination angle $\theta_0 = 90^\circ$.

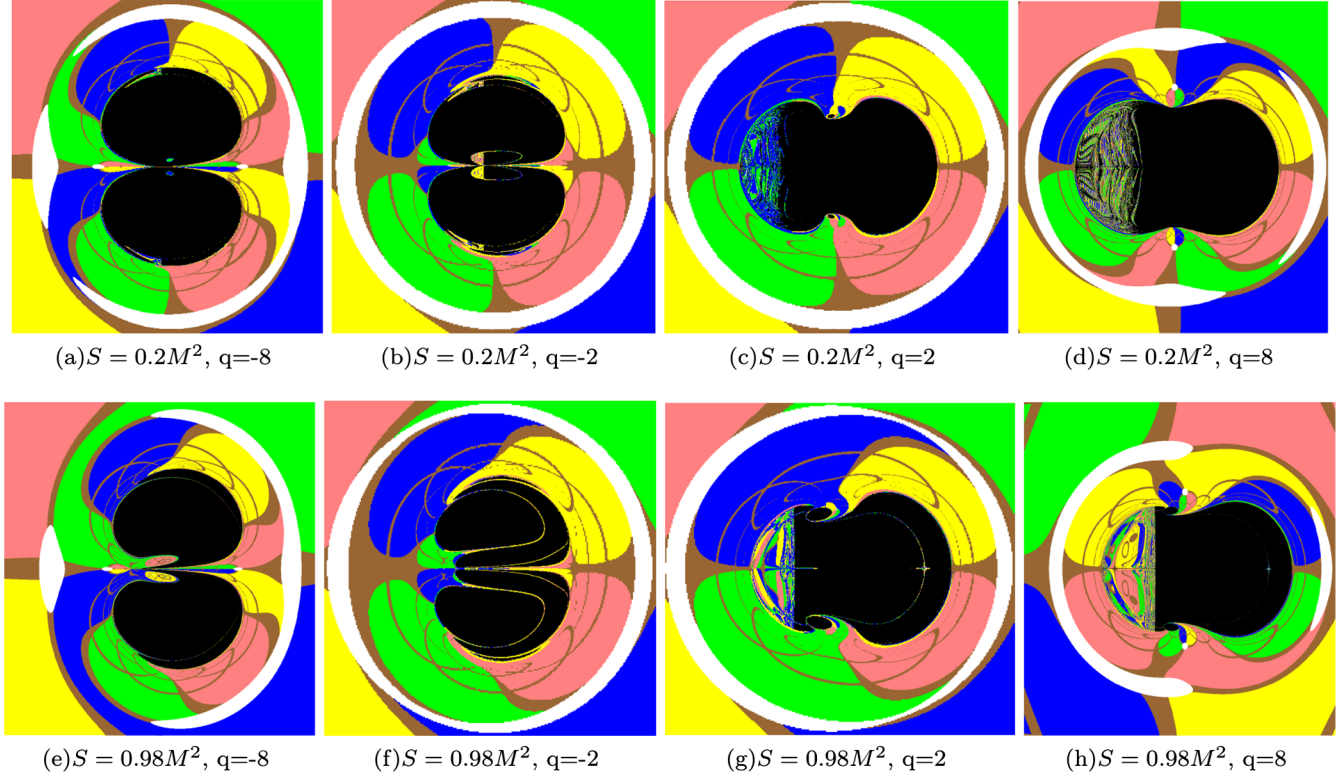


FIG. 4. The change of Einstein ring (white ring in the figures) with the quadrupole-deviation parameter q in the non-Kerr rotating black hole spacetime with a quadrupole mass moment.

TABLE I. The critical value of quadrupole-deviation parameter q_c accounting for a broken Einstein ring in the non-Kerr rotating black hole spacetime with a quadrupole mass moment for different rotation parameter S .

$S(M^2)$	0.1	0.2	0.3	0.4	0.5	0.6	0.7	0.8	0.9	0.98
$q_c(q > 0)$	7.83	7.25	6.65	6.04	5.44	4.81	4.19	3.51	2.82	2.24
$q_c(q < 0)$	-7.83	-7.46	-7.05	-6.61	-6.14	-5.63	-5.06	-4.44	-3.72	-3.07

broken so that the shadows possess an axial symmetric image as $\theta_{\text{obs}} = 90^\circ$. Those properties are similar to those in the Kerr black hole. However, we also find that as $\theta_{\text{obs}} = 0^\circ$, there are concentric bright rings imbedded in the black shadow, which is not appeared in the Kerr black hole case. These distinct features in the shadow can be attributed to the effect of the quadrupole mass moment on the spacetime structures.

IV. OBSERVATIONAL PARAMETERS FOR SHADOW OF A NON-KERR ROTATING BLACK HOLE WITH QUADRUPOLE MASS MOMENT

In this section, supposing that the gravitational field of the supermassive black hole at the Galactic center of the Milky Way can be described by the non-Kerr rotating black hole with a quadrupole mass moment, we estimate the numerical values of observables for the black hole shadow, and then we study the effect of the quadrupole-deviation parameter q on these observables.

To characterize the shadow of a non-Kerr rotating black hole with a quadrupole mass moment, we adopt six observables: the radius R_s , the oblateness parameter K_s , the three dimensionless distortion parameters ($\delta_{s,I}$, $\delta_{s,II}$, and $\delta_{s,III}$) proposed in Ref. [46], and the “thickness” parameter T of the shadow. The former two observables R_s and K_s can be characterized by the points: the top position (x_t, y_t) , the bottom position (x_b, y_b) , the leftmost position (x_l, y_l) , and the rightmost position (x_r, y_r) of the shadow. The observable R_s is defined as in Ref. [35]

$$R_s = \frac{(x_t - x_r)^2 + y_t^2}{2|x_t - x_r|}, \quad (35)$$

and the oblateness parameter K_s of the shadow can be defined as

$$K_s \equiv \frac{\Delta x}{\Delta y} = \frac{x_r - x_l}{y_t - y_b}. \quad (36)$$

If a shadow is a standard circle, we find $K_s = 1$. Moreover, the oblateness parameter satisfies $K_s > 1$ for the case in which the contour of the shadow is oblate, and $K_s < 1$ for the case in which the shadow is prolate.

To describe further general characterization of the shadow, A. Abdujabbarov *et al.* [46] expanded the polar curve R_ψ representing the shadow as Legendre polynomials,

i.e., $R_\psi = \sum_{l=0}^{\infty} c_l P_l(\cos \psi)$, and defined three dimensionless distortion parameters,

$$\begin{aligned} \delta_{s,I} &\equiv \frac{2 \sum_{l=1}^{\infty} c_{2l-1}}{\mathcal{B}}, \\ \delta_{s,II} &\equiv \frac{2(\mathcal{B}^2 - \mathcal{A}\mathcal{C})}{\mathcal{B}^2 + \mathcal{A}^2}, \\ \delta_{s,III} &\equiv 2 \left(\sum_{l=0}^{\infty} c_l P_l(x_S) \right) \\ &\times \frac{\sum_{l=0}^{\infty} c_l P_l(x_S) - x_S \sum_{l=1}^{\infty} c_{2l-1} - \mathcal{A}\mathcal{C}}{\mathcal{A}^2 - 2x_S \sum_{l=0}^{\infty} c_l P_l(x_S) + (\sum_{l=0}^{\infty} c_l P_l(x_S))^2}, \end{aligned} \quad (37)$$

where

$$\begin{aligned} \mathcal{A} &\equiv R_\psi(\psi = 0) = \sum_{l=0}^{\infty} c_l, \\ \mathcal{B} &\equiv R_\psi(\psi = \pi/2) = \sum_{l=0}^{\infty} (-1)^l \frac{(2l)!}{2^{2l}(l!)^2} c_{2l}, \\ \mathcal{C} &\equiv R_\psi(\psi = \pi) = \sum_{l=0}^{\infty} (-1)^l c_l. \end{aligned} \quad (38)$$

and $x_S = \cos \psi_S$, which obeys the condition

$$\frac{dR_\psi}{d\psi} \sin \psi + R_\psi \cos \psi = 0. \quad (39)$$

For the aim of describing the multiple shadows appearing in Figs. 1–5, we can scan across the shadow along a certain line (such as image coordinate $x = \text{const}$) from the bottommost border of the shadow to the equatorial plane and then define the thickness parameter T as

$$T \equiv \sum_{i=1}^n l_i, \quad (40)$$

where l_i is the width of i th black shadow along the selected scan line and n is total number of shadows. If there is only a single shadow, T is a linear function of the image coordinate variable y as we scan across the shadow along an arbitrary line. If there exist multiple shadows, one can find a scan line at least so that some platforms appear in the curve of $T(y)$, which can be called the “plateau effect”

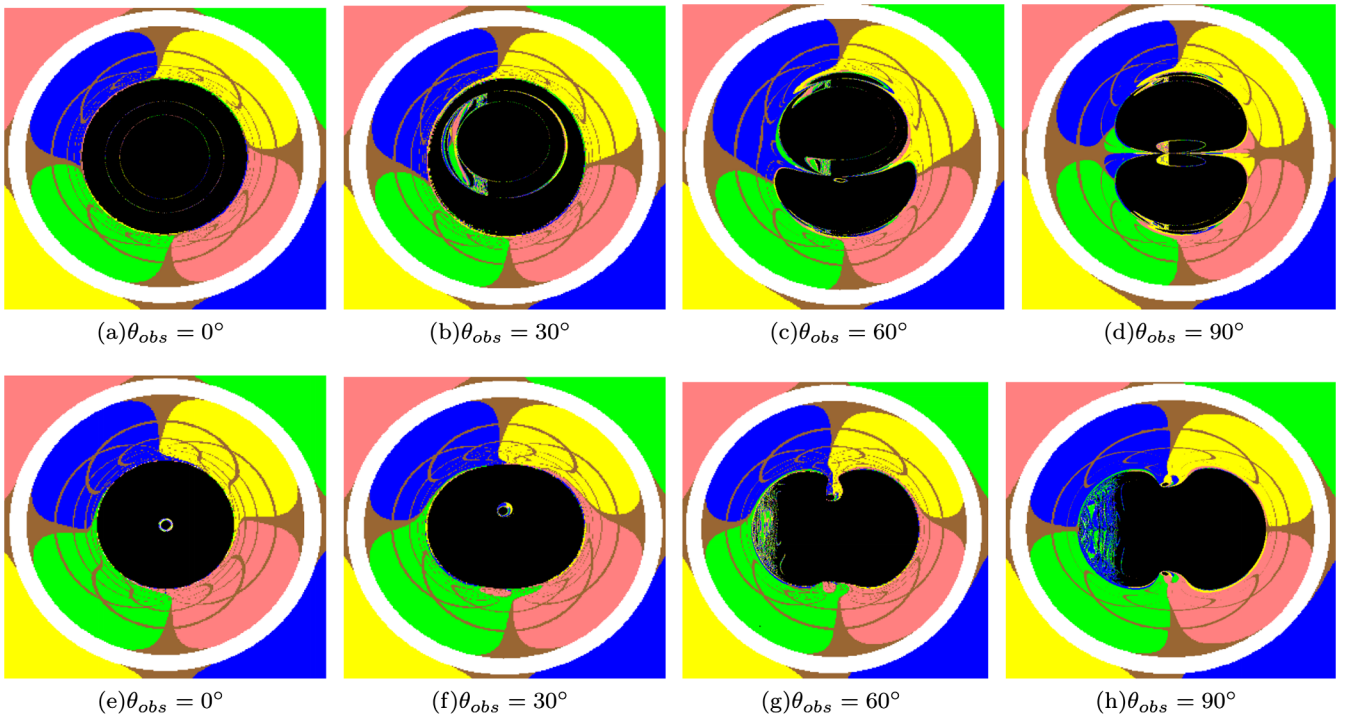


FIG. 5. The shadow of a non-Kerr rotating compact object with a quadrupole mass moment for different observer's inclination angles $\theta_{obs} = 0^\circ, 30^\circ, 60^\circ, 90^\circ$. The top row is for the quadrupole-deviation parameter $q = -2$, and the bottom row is for $q = 2$. Here, we set $M = 1$ and $S = 0.2M^2$.

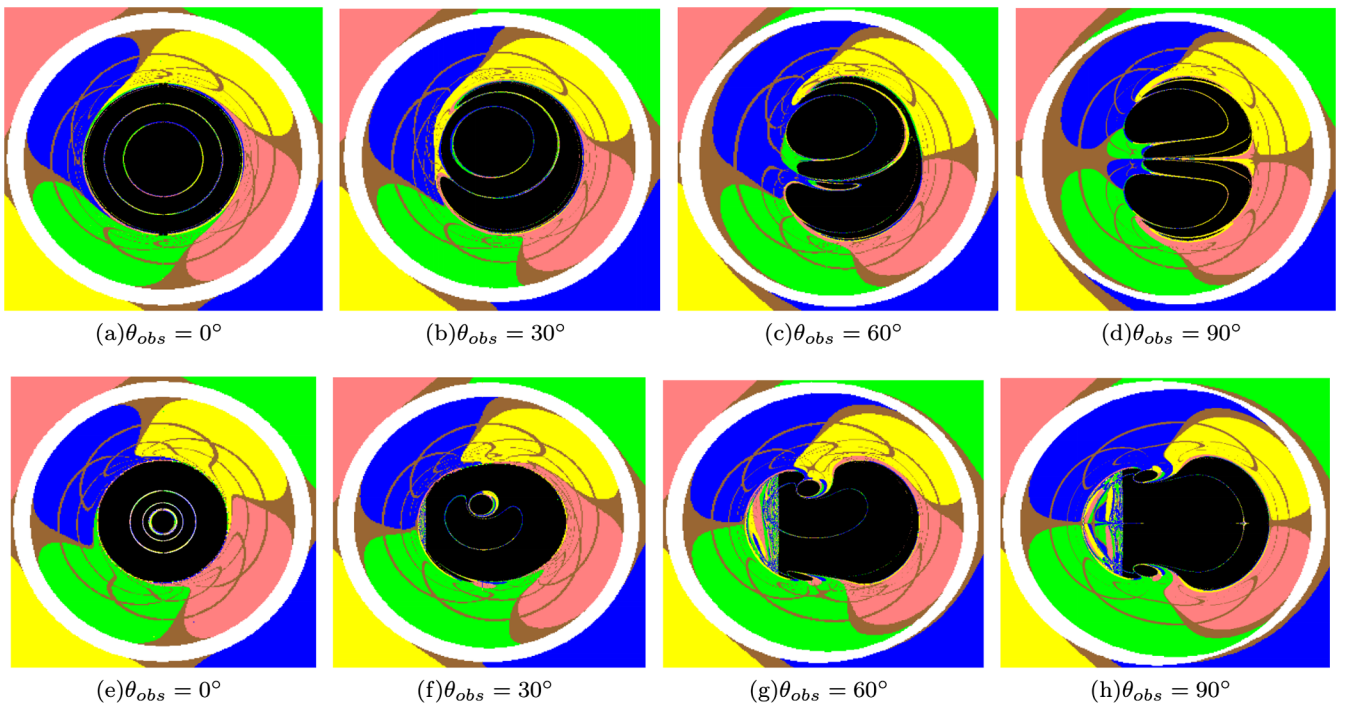


FIG. 6. The shadow of a non-Kerr rotating compact object with a quadrupole mass moment for different observer's inclination angles $\theta_{obs} = 0^\circ, 30^\circ, 60^\circ, 90^\circ$. The top row is for the quadrupole-deviation parameter $q = -2$, and the bottom row is for $q = 2$. Here, we set $M = 1$ and $S = 0.98M^2$.

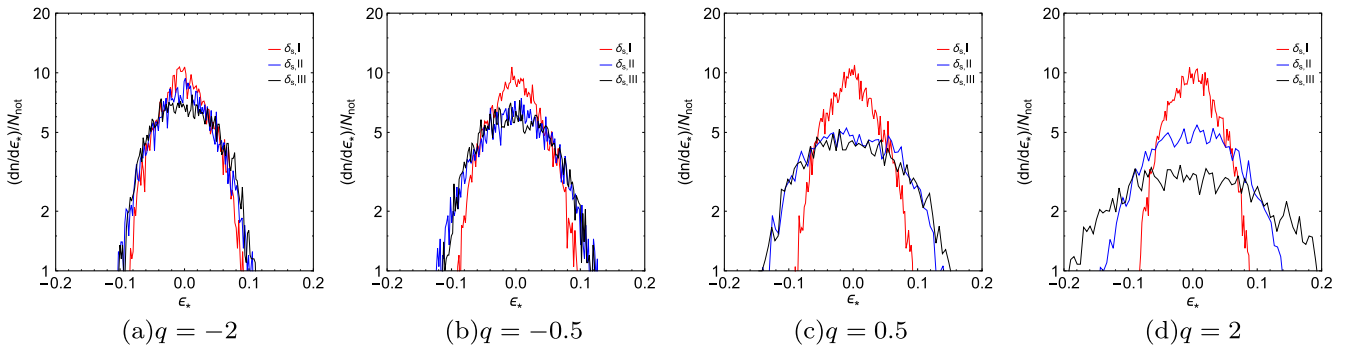


FIG. 7. The probability density distributions of the measurement errors ϵ_* of three distortion parameters $\delta_{s,I}$, $\delta_{s,II}$, $\delta_{s,III}$ for the shadow of a non-Kerr rotating compact object with a quadrupole mass moment $q = -2$, 0.5 , 0.5 , 2 , and we set spin parameter $S = 0.2M^2$.

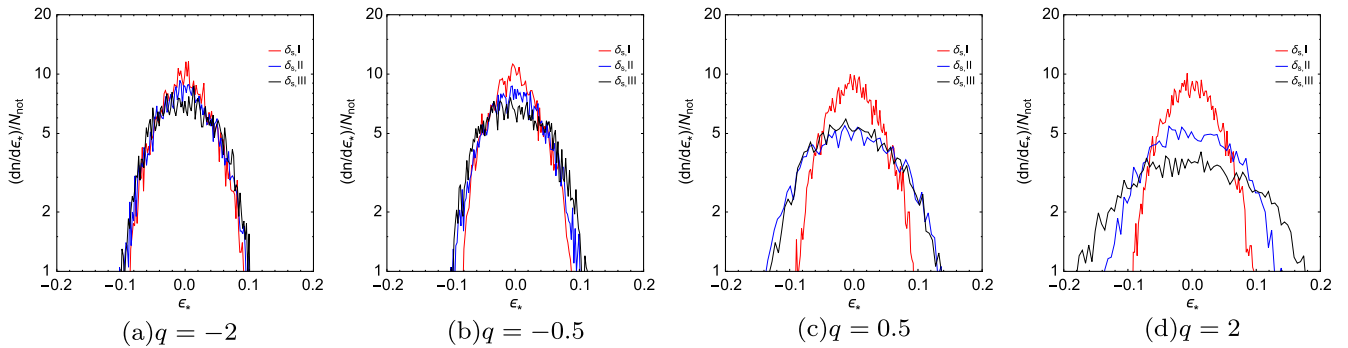


FIG. 8. The probability density distributions of the measurement errors ϵ_* of three distortion parameters $\delta_{s,I}$, $\delta_{s,II}$, $\delta_{s,III}$ for the shadow of a non-Kerr rotating compact object with a quadrupole mass moment $q = -2$, 0.5 , 0.5 , 2 , and we set spin parameter $S = 0.98M^2$.

(see in Figs. 9–12). The fractal structures in these platforms' distribution can be regarded as a potential observable effect of chaotic lensing.

The mass of the central object of our Galaxy is estimated to be $4.4 \times 10^6 M_\odot$, and its distance is around 8.5 kpc [59]. In Tables II and III, we present the numerical values of observables R_s and K_s and the magnitudes of three distortion parameters $\delta_{s,I}$, $\delta_{s,II}$, and $\delta_{s,III}$ for the shadow of the supermassive black hole at the Galactic center of the Milky Way by applying the metric of the non-Kerr rotating black hole with a quadrupole mass moment (18) as the observer's inclination angle is $\theta_{\text{obs}} = 90^\circ$ for different q and S . Tables II and III indicate that these observables are functions of black hole parameters q and S . For fixed spin parameter S , one can find that R_s decreases with $|q|$ for the negative quadrupole-deviation parameter, but it first decreases and then increases for the positive one. The oblateness parameter K_s decreases with $|q|$ for the negative q . For the case with positive q , the change of K_s with q depends on the value of spin parameter S . Moreover, from Tables II and III, one can find that $\delta_{s,I}$ first increases and then decreases with $|q|$ in both cases $S = 0.2$ and $S = 0.98$.

The changes of $\delta_{s,II}$ and $\delta_{s,III}$ with q become more complicated. For the negative q , the quantities $\delta_{s,II}$ and $\delta_{s,III}$ increase with $|q|$. For positive q , $\delta_{s,II}$ and $\delta_{s,III}$ first increase and then decrease with q in the case $S = 0.2$, but they first decrease and then increase and finally decrease with q in the case $S = 0.98$. Because of the existence of intrinsic uncertainties in astronomical observations, the white noise could appear in the observational data for shadow's polar curve R_ψ . With the method proposed by A. Abdujabbarov *et al.* [46], we also analyze the observational random errors in the measurements of the shadow. In Figs. 7 and 8, we present the probability density distributions of the measurement errors $\epsilon_* = \delta_s - \delta_{s,*}$ for three distortion parameters $\delta_{s,I}$, $\delta_{s,II}$, and $\delta_{s,III}$ with different q and S . Here, δ_s is the exact distortion of the background metric (18), and the index $* = I, II, III$, respectively, corresponds to the case of $\delta_{s,I}$, $\delta_{s,II}$ and $\delta_{s,III}$. As in Ref. [46], we find that all the distributions of the measurement errors are centered on $\epsilon_* = 0$, and there is the smallest error variation for the distortion parameter $\delta_{s,I}$. Moreover, we find that the variance of the distortion parameters $\delta_{s,I}$, $\delta_{s,II}$, and $\delta_{s,III}$ increases with quadrupole-deviation parameter q .

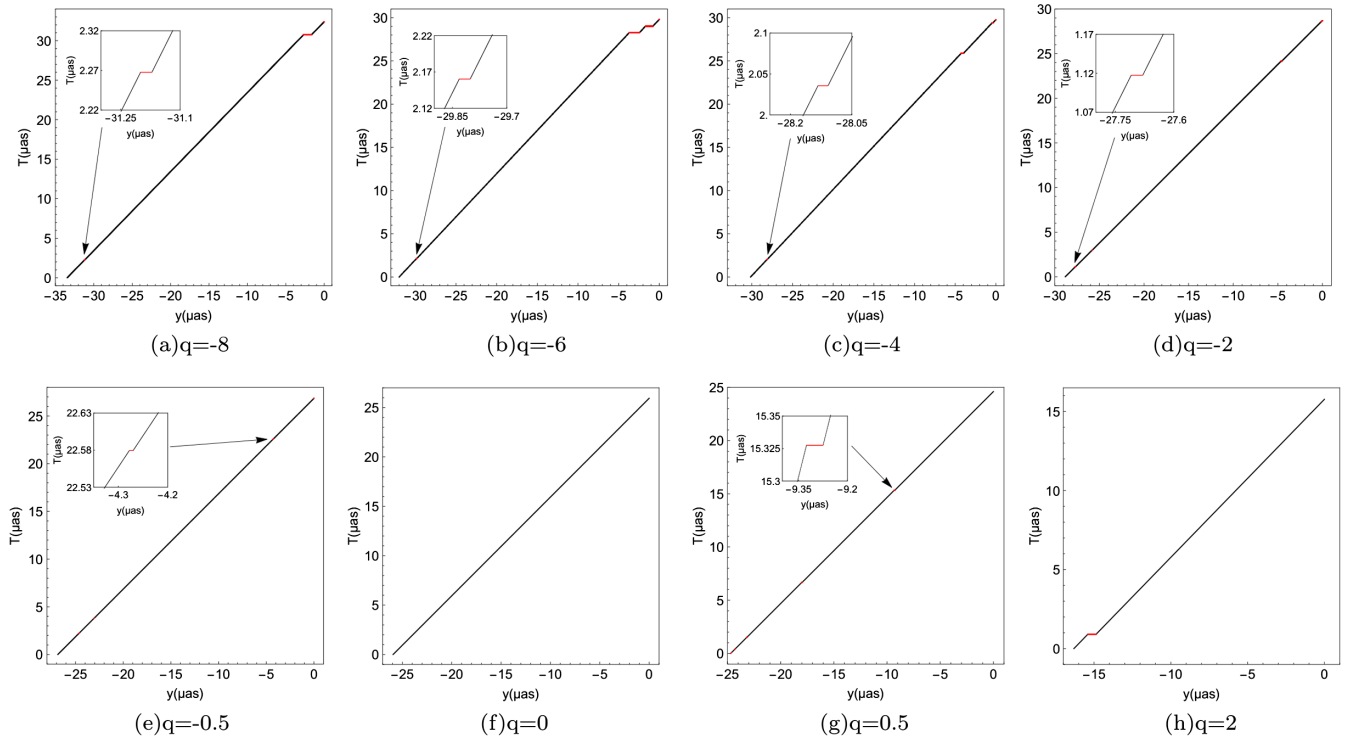


FIG. 9. The curves of $T(y)$ with quadrupole mass moment $q = -8, -6, -4, -2, -0.5, 0, 0.5, 2$ for the fixed spin parameter $S = 0.2M^2$ as we scan across the shadow along the line $x = 0$. Here, we set observer's inclination angle $\theta_{\text{obs}} = 90^\circ$.

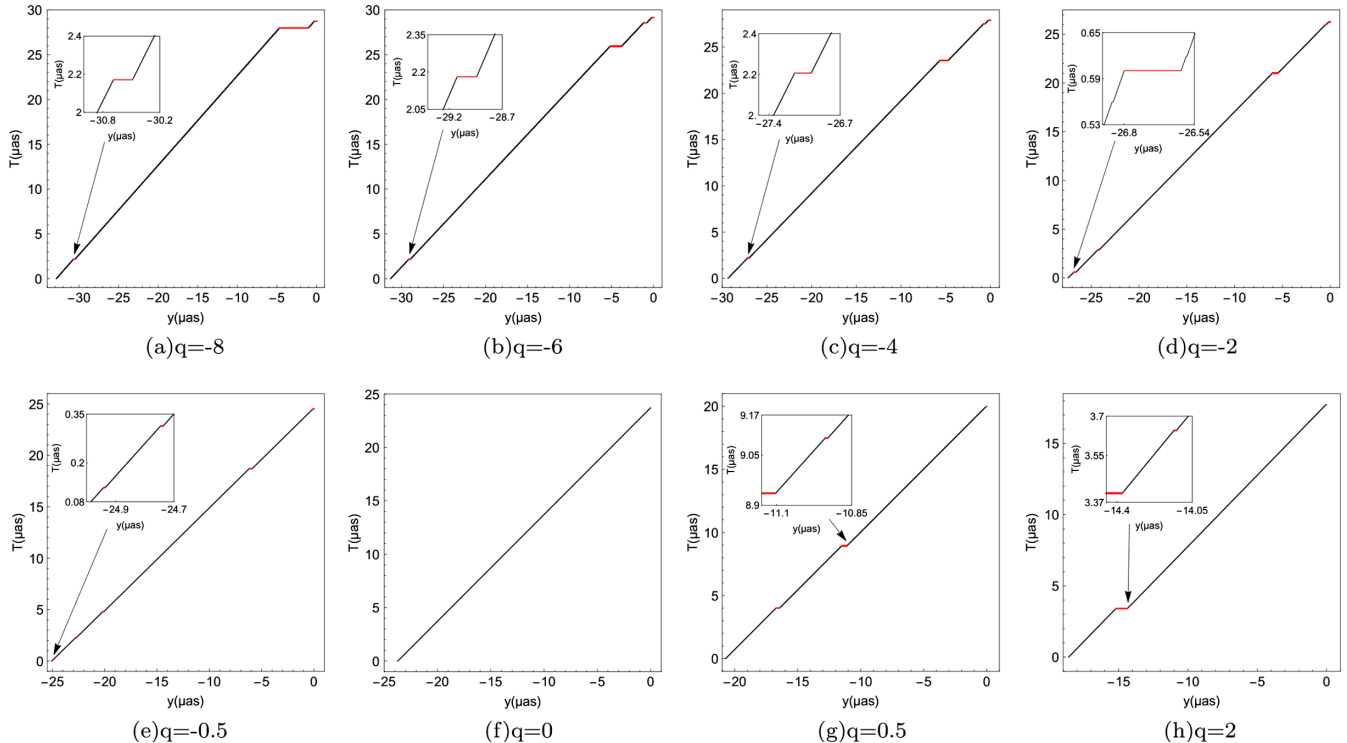


FIG. 10. The curves of $T(y)$ with quadrupole mass moment $q = -8, -6, -4, -2, -0.5, 0, 0.5, 2$ for the fixed spin parameter $S = 0.98M^2$ as we scan across the shadow along the line $x = 0$. Here, we set the observer's inclination angle $\theta_{\text{obs}} = 90^\circ$.

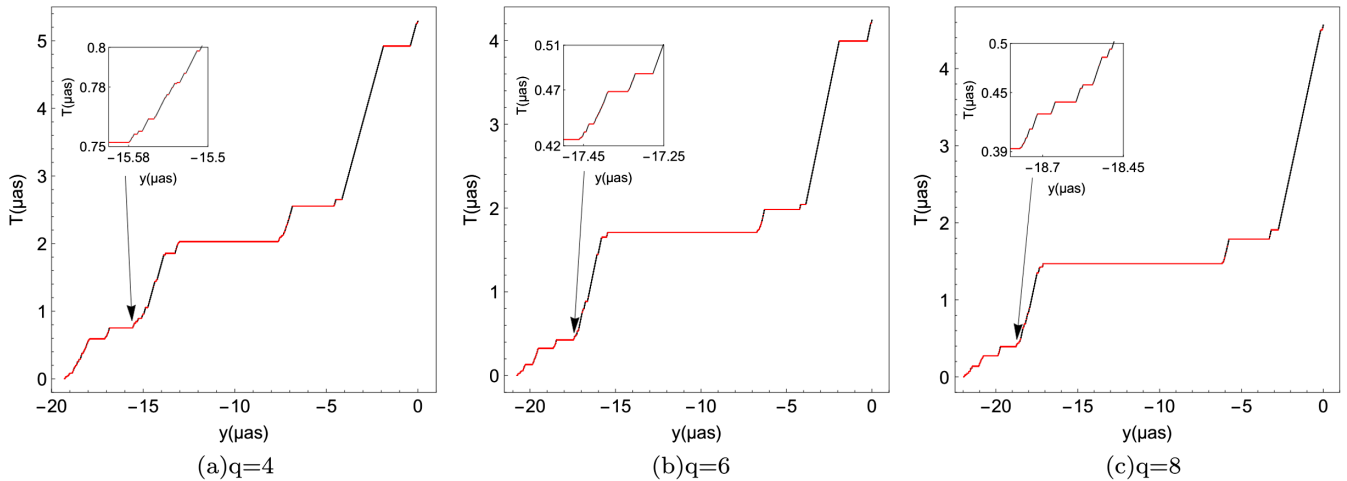


FIG. 11. The curves of $T(y)$ with quadrupole mass moment $q = 4, 6, 8$ for the fixed spin parameter $S = 0.2M^2$ as we scan across the shadow along the line $x = -4$. Here, we set the observer's inclination angle $\theta_{\text{obs}} = 90^\circ$.

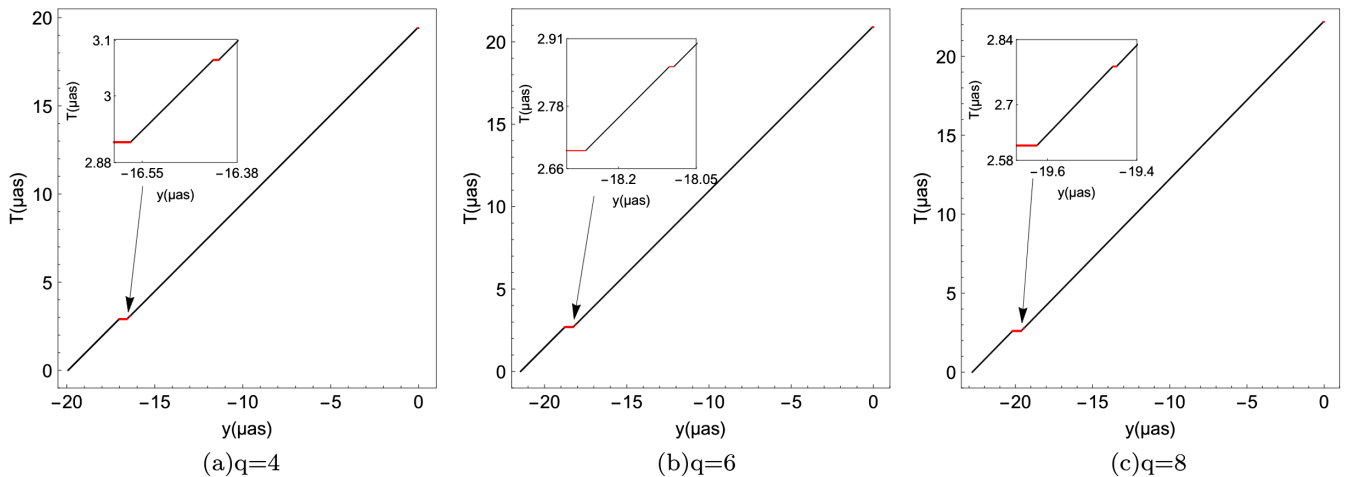


FIG. 12. The curves of $T(y)$ with quadrupole mass moment $q = -8, -6, -4, -2, -0.5, 0, 0.5, 2$ for the fixed spin parameter $S = 0.98M^2$ as we scan across the shadow along the line $x = -0.5$. Here, we set the observer's inclination angle $\theta_{\text{obs}} = 90^\circ$.

In Figs. 9–12, we plot the curve of thickness parameter $T(y)$ for different q and S . For the case with $q = 0$, there is only a single shadow for the black hole, and we find that thickness parameter T increases linearly with the variable y without any platform. For the cases with $q \neq 0$, we find that there exist some platforms in the curve of thickness parameter $T(y)$, which correspond to the bright region in the pattern of the black hole shadow in which the light is not captured by the black hole so that it can reach the observer. In Figs. 9 and 10, we scan across the shadow along the line $x = 0$ and find that the platforms appear in the cases with the quadrupole-deviation parameter $q = -8, -6, -4, -2, -0.5, 0, 0.5, 2$. For the cases with $q = 4, 6, 8$, we find that there exist also the platforms as we select the scan line $x = -4$ for $S = 0.2M^2$ and the line $x = -0.5$ for $S = 0.98M^2$. The width, positions, and numbers of platforms depend on black hole parameters. The fractal

structure in the platform set actually reflects a self-similar feature of multiple shadows caused by chaotic lensing. These platform distribution could also provide a potential observable signal identified photon chaotic motion through black hole shadows. Theoretically, comparing the theoretical values of these observables R_s and K_s ; three distortion parameters $\delta_{s,I}$, $\delta_{s,II}$, and $\delta_{s,III}$; and T with those observation values obtained by astronomical instruments, one can extract the black hole information including the spin parameter S and the quadrupole-deviation parameter q from the black hole shadow. However, we note that resolutions of less than $0.1\mu\text{as}$ are needed in order to extract useful information from observations of the shadow of the supermassive black hole at the Galactic center of the Milky Way, which is impossible for the current observational experiments, even for the most sensitive measurements, such as the Event Horizon Telescope [17,18] and

TABLE II. Numerical values of observables R_s and K_s and three distortion parameters $\delta_{s,I}$, $\delta_{s,II}$, and $\delta_{s,III}$ for the shadow of the supermassive black hole at the Galactic center of the Milky Way with the metric of the non-Kerr rotating black hole with a quadrupole mass moment as the observer's inclination angle is $\theta_{\text{obs}} = 90^\circ$ for the fixed spin parameter $S = 0.2M^2$.

q	-8	-6	-4	-2	-0.5	0	0.5	2	4	6	8
$x_l(\mu\text{as})$	-22.48	-21.97	-20.95	-20.44	-20.29	-23.91	-26.06	-14.46	-12.26	-11.24	-10.99
$y_l(\mu\text{as})$	± 14.15	± 13.03	± 11.75	± 9.96	± 6.34	0	0	0	0	0	0
$x_r(\mu\text{as})$	25.14	24.53	24.02	23.50	24.07	28.10	29.64	32.60	34.75	36.79	38.94
$y_r(\mu\text{as})$	± 14.31	± 12.77	± 11.50	± 9.71	± 4.85	0	0	0	0	0	0
$x_t, x_b(\mu\text{as})$	0.05	0.92	1.28	1.64	2.04	2.55	2.76	13.34	15.84	16.61	16.86
$y_t, -y_b(\mu\text{as})$	33.42	31.68	30.15	28.97	26.98	26.06	24.83	21.46	21.46	22.48	23.35
$\Delta x(\mu\text{as})$	47.62	46.50	44.97	43.94	44.35	52.02	55.70	47.06	47.26	48.03	49.92
$\Delta y(\mu\text{as})$	66.84	63.36	60.29	57.94	53.96	52.12	49.67	42.92	42.92	44.97	46.70
K_s	0.71	0.73	0.75	0.76	0.82	0.998	1.12	1.096	1.095	1.068	1.069
$R_s(\mu\text{as})$	34.80	33.06	31.36	30.13	27.54	26.07	24.91	21.59	21.63	22.61	23.39
$\delta_{s,I}$	0.1889	0.2345	0.2892	0.2106	0.0510	0.0021	0.1144	0.1377	0.1932	0.1869	0.1809
$\delta_{s,II}$	0.7661	0.6100	0.5697	0.5560	0.3841	0.0042	0.2457	0.3176	0.4476	0.3815	0.3658
$\delta_{s,III}$	0.6658	0.5434	0.5116	0.4968	0.3500	0.0045	0.2612	0.3870	0.8687	0.6712	0.5881

TABLE III. Numerical values of observables R_s and K_s and three distortion parameters $\delta_{s,I}$, $\delta_{s,II}$, and $\delta_{s,III}$ for the shadow of the supermassive black hole at the Galactic center of the Milky Way with the metric of the non-Kerr rotating black hole with a quadrupole mass moment as the observer's inclination angle is $\theta_{\text{obs}} = 90^\circ$ for the fixed spin parameter $S = 0.98M^2$.

q	-8	-6	-4	-2	-0.5	0	0.5	2	4	6	8
$x_l(\mu\text{as})$	-16.86	-15.84	-14.82	-13.18	-10.73	-11.75	-9.71	-9.71	-9.71	-9.81	-9.86
$y_l(\mu\text{as})$	± 14.31	± 13.29	± 12.52	± 11.24	± 9.20	0	0	0	0	0	0
$x_r(\mu\text{as})$	29.79	29.13	29.13	29.23	33.93	35.26	36.28	38.53	40.37	42.41	43.94
$y_r(\mu\text{as})$	± 14.21	± 13.29	± 11.24	± 8.43	± 0.10	0	0	0	0	0	0
$x_t, x_b(\mu\text{as})$	7.26	7.46	7.66	7.92	8.89	10.07	13.29	18.29	20.95	21.46	21.77
$y_t, -y_b(\mu\text{as})$	33.72	32.19	30.15	28.97	27.08	26.06	24.78	23.30	22.99	24.02	24.73
$\Delta x(\mu\text{as})$	46.65	44.97	43.94	42.41	44.66	47.01	45.99	48.24	50.08	52.22	53.81
$\Delta y(\mu\text{as})$	67.45	64.38	60.29	57.94	54.16	52.12	49.56	46.60	45.99	48.03	49.46
K_s	0.69	0.70	0.73	0.73	0.82	0.90	0.93	1.04	1.089	1.087	1.088
$R_s(\mu\text{as})$	36.50	34.74	31.90	30.35	27.16	26.08	24.85	23.53	23.32	24.24	24.88
$\delta_{s,I}$	0.2094	0.2730	0.2207	0.2096	0.1418	0.1073	0.1110	0.2155	0.2079	0.1945	0.1869
$\delta_{s,II}$	0.7087	0.6950	0.6318	0.6400	0.4925	0.2124	0.1324	0.1537	0.2120	0.2002	0.1849
$\delta_{s,III}$	0.6188	0.6077	0.5588	0.5649	0.4605	0.2108	0.1315	0.8386	0.7024	0.5728	0.4795

European Black Hole Cam [19]. We expect that it will reach in the future with the development of observation technology.

V. SUMMARY

With the technique of backward ray tracing, we have numerically studied the shadows of a non-Kerr rotating compact object with an extra parameter related to the quadrupole mass moment, which describes the deviation from the Kerr black hole. Our results show that the shadows of a non-Kerr rotating compact object depend sharply on the quadrupole-deviation parameter q and the rotation parameter S . For the case with negative q , the shadow of the non-Kerr rotating compact object with a quadrupole mass moment becomes prolate, and it is split into two disconnected main shadows with eyebrows, which lie at symmetric positions above and below the equatorial plane.

With the increase of the deviation, the curvature of the boundary line near the equatorial plane increases for the main shadow. For the case with positive q , we found that the shadow of the non-Kerr rotating compact object with a quadrupole mass moment becomes oblate and the main shadows are joined together in the equatorial plane. With the increase of the deviation, the shadow becomes oblate so that it turns into the shape of a dumbbell for the larger q . In addition, there is a disorder region in the left of shadow which increases with the quadrupole-deviation parameter q . Interestingly, we also found that the Einstein ring is broken for the absolute value of q more than a certain critical value $|q_c|$. The critical value $|q_c|$ decreases with the rotation parameter of a non-Kerr rotating black hole. We also discussed the dependence of the shadow on the observer's inclination angle θ_{obs} . Especially, as $\theta_{\text{obs}} = 0^\circ$, there are concentric bright rings appearing in the black disk. Our results show that the presence of the quadrupole mass

moment yields a series of interesting patterns for the shadow of a non-Kerr rotating compact object with a quadrupole mass moment.

The model was applied to the supermassive black hole in the Galactic center. Our results show that for fixed spin parameter S one can find that the observable R_s decreases with $|q|$ for the negative quadrupole-deviation parameter, but it first decreases and then increases for the positive one. The oblateness parameter K_s decreases with $|q|$ for negative q . For the case with positive q , the change of K_s with q depends on the value of spin parameter S . We also studied the effects of q on the magnitudes of three distortion parameters $\delta_{s,I}$, $\delta_{s,II}$, and $\delta_{s,III}$ for the shadow and analyzed the probability density distributions of the measurement errors ϵ_* for these distortion parameters with different q and S . Finally, we note that there exist some

platforms in the curve of thickness parameter $T(y)$, which correspond to the regions in which the light is not captured by black hole and can reach the observer. The width, positions, and numbers of these platforms depend on black hole parameters.

ACKNOWLEDGMENTS

We would like to thank the referee for useful comments. This work was partially supported by the National Natural Science Foundation of China under Grant No. 11875026 and the Scientific Research Fund of Hunan Provincial Education Department Grant No. 17A124. J. J. work was partially supported by the National Natural Science Foundation of China under Grants No. 11475061 and No. 11875025.

-
- [1] B. P. Abbott *et al.* (LIGO Scientific and Virgo Collaborations), Observation of Gravitational Waves from a Binary Black Hole Merger, *Phys. Rev. Lett.* **116**, 061102 (2016).
 - [2] B. Abbott *et al.* (LIGO Scientific and Virgo Collaborations), GW151226: Observation of Gravitational Waves from a 22-Solar-Mass Binary Black Hole Coalescence, *Phys. Rev. Lett.* **116**, 241103 (2016).
 - [3] B. Abbott *et al.* (LIGO Scientific and Virgo Collaborations), GW170104: Observation of a 50-Solar-Mass Binary Black Hole Coalescence at Redshift 0.2, *Phys. Rev. Lett.* **118**, 221101 (2017).
 - [4] B. Abbott *et al.* (LIGO Scientific and Virgo Collaborations), GW170814: A Three-Detector Observation of Gravitational Waves from a Binary Black Hole Coalescence, *Phys. Rev. Lett.* **119**, 141101 (2017).
 - [5] B. Abbott *et al.* (LIGO Scientific and Virgo Collaborations), GW170608: Observation of a 19 solar-mass binary black hole coalescence, *Astrophys. J.* **851**, L35 (2017).
 - [6] W. Israel, Event horizons in static vacuum space-times, *Phys. Rev.* **164**, 1776 (1967); Event horizons in static electrovac space-times, *Commun. Math. Phys.* **8**, 245 (1968); B. Carter, Axisymmetric Black Hole has only Two Degrees of Freedom, *Phys. Rev. Lett.* **26**, 331 (1971); S. W. Hawking, Black holes in general relativity, *Commun. Math. Phys.* **25**, 152 (1972); D. C. Robinson, Uniqueness of the Kerr Black Hole, *Phys. Rev. Lett.* **34**, 905 (1975).
 - [7] T. Johannsen and D. Psaltis, A metric for rapidly spinning black holes suitable for strong-field tests of the no-hair theorem, *Phys. Rev. D* **83**, 124015 (2011).
 - [8] R. Konoplya and A. Zhidenko, Detection of gravitational waves from black holes: Is there a window for alternative theories?, *Phys. Lett. B* **756**, 350 (2016).
 - [9] R. Konoplya, L. Rezzolla, and A. Zhidenko, General parametrization of axisymmetric black holes in metric theories of gravity, *Phys. Rev. D* **93**, 064015 (2016).
 - [10] V. S. Manko and I. D. Novikov, Generalizations of the Kerr and Kerr-Newman metrics possessing an arbitrary set of massmultipole moments, *Classical Quantum Gravity* **9**, 2477 (1992).
 - [11] J. R. Gair, Observable properties of orbits in exact bumpy spacetimes, *Phys. Rev. D* **77**, 024035 (2008).
 - [12] G. Lukes-Gerakopoulos, T. A. Apostolatos, and G. Contopoulos, An observable signature of a background deviating from Kerr, *Phys. Rev. D* **81**, 124005 (2010).
 - [13] G. Lukes-Gerakopoulos, G. Contopoulos, and T. A. Apostolatos, Non-linear effects in non-Kerr spacetimes, *Proc. Phys.* **157**, 129 (2014).
 - [14] J. L. Synge, The escape of photons from gravitationally intense stars, *Mon. Not. R. Astron. Soc.* **131**, 463 (1966).
 - [15] J. M. Bardeen, Timelike and null geodesics in the Kerr metric, in *Black Holes (Les Astres Occlus)*, edited by C. DeWitt and B. DeWitt (Gordon and Breach, New York, 1973), p. 215.
 - [16] S. Chandrasekhar, *The Mathematical Theory of Black Holes* (Oxford University, New York, 1992).
 - [17] S. Doeleman *et al.*, Event-horizon-scale structure in the supermassive black hole candidate at the Galactic Centre, *Nature (London)* **455**, 78 (2008).
 - [18] Y. Mizuno, Z. Younsi, C. M. Fromm, O. Porth, M. D. Laurentis, H. Olivares, H. Falcke, M. Kramer, and L. Rezzolla, The current ability to test theories of gravity with black hole shadows, *Nature Astronomy* **2**, 585 (2018).
 - [19] C. Goddi *et al.*, BlackHoleCam: fundamental physics of the Galactic Center, *Int. J. Mod. Phys. D* **26**, 1730001 (2017).
 - [20] P. V. P. Cunha, C. Herdeiro, and E. Radu, Fundamental photon orbits: Black hole shadows and spacetime instabilities, *Phys. Rev. D* **96**, 024039 (2017).
 - [21] M. Wang, S. Chen, and J. Jing, Shadow casted by a Konoplya-Zhidenko rotating non-Kerr black hole, *J. Cosmol. Astropart. Phys.* **10** (2017) 051.

- [22] P. V. P. Cunha, C. Herdeiro, E. Radu, and H. F. Runarsson, Shadows of Kerr Black Holes with Scalar Hair, *Phys. Rev. Lett.* **115**, 211102 (2015).
- [23] P. V. P. Cunha, C. Herdeiro, E. Radu, and H. F. Runarsson, Shadows of Kerr black holes with and without scalar hair, *Int. J. Mod. Phys. D* **25**, 1641021 (2016).
- [24] F. H. Vincent, E. Gourgoulhon, C. Herdeiro, and E. Radu, Astrophysical imaging of Kerr black holes with scalar hair, *Phys. Rev. D* **94**, 084045 (2016).
- [25] P. V. P. Cunha, J. Grover, C. Herdeiro, E. Radu, H. Runarsson, and A. Wittig, Chaotic lensing around boson stars and Kerr black holes with scalar hair, *Phys. Rev. D* **94**, 104023 (2016).
- [26] J. O. Shipley and S. R. Dolan, Binary black hole shadows, chaotic scattering and the Cantor set, *Classical Quantum Gravity* **33**, 175001 (2016).
- [27] A. Bohn, W. Throwe, F. Hbert, K. Henriksson, and D. Bunandar, What does a binary black hole merger look like?, *Classical Quantum Gravity* **32**, 065002 (2015).
- [28] M. Wang, S. Chen, and J. Jing, Shadows of a compact object with magnetic dipole by chaotic lensing, *Phys. Rev. D* **97**, 064029 (2018).
- [29] J. Grover and A. Wittig, Black hole shadows and invariant phase space structures, *Phys. Rev. D* **96**, 024045 (2017).
- [30] T. Johannsen, Photon rings around Kerr and Kerr-like black holes, *Astrophys. J.* **777**, 170 (2013).
- [31] H. Falcke, F. Melia, and E. Agol, Viewing the shadow of the black hole at the Galactic Center, *Astrophys. J.* **528**, L13 (2000).
- [32] A. de Vries, The apparent shape of a rotating charged black hole, closed photon orbits and the bifurcation set A_4 , *Classical Quantum Gravity* **17**, 123 (2000).
- [33] R. Takahashi, Shapes and positions of black hole shadows in accretion disks and spin parameters of black holes, *Astrophys. J.* **611**, 996 (2004).
- [34] C. Bambi and K. Freese, Apparent shape of super-spinning black holes, *Phys. Rev. D* **79**, 043002 (2009); Z. Li and C. Bambi, Measuring the Kerr spin parameter of regular black holes from their shadow, *J. Cosmol. Astropart. Phys.* **01** (2014) 041.
- [35] K. Hioki and K. I. Maeda, Measurement of the Kerr spin parameter by observation of a compact object's shadow, *Phys. Rev. D* **80**, 024042 (2009).
- [36] L. Amarilla, E. F. Eiroa, and G. Giribet, Null geodesics and shadow of a rotating black hole in extended Chern-Simons modified gravity, *Phys. Rev. D* **81**, 124045 (2010).
- [37] L. Amarilla and E. F. Eiroa, Shadow of a rotating braneworld black hole, *Phys. Rev. D* **85**, 064019 (2012).
- [38] A. Yumoto, D. Nitta, T. Chiba, and N. Sugiyama, Shadows of multi-black holes: Analytic exploration, *Phys. Rev. D* **86**, 103001 (2012).
- [39] L. Amarilla and E. F. Eiroa, Shadow of a Kaluza-Klein rotating dilaton black hole, *Phys. Rev. D* **87**, 044057 (2013).
- [40] P. G. Nedkova, V. Tinchev, and S. S. Yazadjiev, The shadow of a rotating traversable wormhole, *Phys. Rev. D* **88**, 124019; V. K. Tinchev and S. S. Yazadjiev, Possible imprints of cosmic strings in the shadows of galactic black holes, *Int. J. Mod. Phys. D* **23**, 1450060 (2014).
- [41] S. W. Wei and Y. X. Liu, Observing the shadow of Einstein-Maxwell-Dilaton-Axion black hole, *J. Cosmol. Astropart. Phys.* **11** (2013) 063.
- [42] V. Perlick, O. Y. Tsupko, and G. S. Bisnovatyi-Kogan, Influence of a plasma on the shadow of a spherically symmetric black hole, *Phys. Rev. D* **92**, 104031 (2015).
- [43] Y. Huang, S. Chen, and J. Jing, Double shadow of a regular phantom black hole as photons couple to Weyl tensor, *Eur. Phys. J. C* **76**, 594 (2016).
- [44] Z. Younsi, A. Zhidenko, L. Rezzolla, R. Konoplya, and Y. Mizuno, A new method for shadow calculations: Application to parameterised axisymmetric black holes, *Phys. Rev. D* **94**, 084025 (2016).
- [45] A. Abdujabbarov, M. Amir, B. Ahmedov, and S. Ghosh, Shadow of rotating regular black holes, *Phys. Rev. D* **93**, 104004 (2016); F. Atamurotov, B. Ahmedov, and A. Abdujabbarov, Optical properties of black hole in the presence of plasma: Shadow, *Phys. Rev. D* **92**, 084005 (2015); A. Abdujabbarov, F. Atamurotov, N. Dadhich, B. Ahmedov, and Z. Stuchlík, Energetics and optical properties of 6-dimensional rotating black hole in pure Gauss-Bonnet gravity, *Eur. Phys. J. C* **75**, 399 (2015); F. Atamurotov, A. Abdujabbarov, and B. Ahmedov, Shadow of rotating non-Kerr black hole, *Phys. Rev. D* **88**, 064004 (2013).
- [46] A. Abdujabbarov, L. Rezzolla, and B. Ahmedov, A coordinate-independent characterization of a black hole shadow, *Mon. Not. R. Astron. Soc.* **454**, 2423 (2015).
- [47] M. Sharif and S. Iftikhar, Shadow of a charged rotating non-commutative black hole, *Eur. Phys. J. C* **76**, 630 (2016).
- [48] N. Tsukamoto, Black hole shadow in an asymptotically-flat, stationary, and axisymmetric spacetime: The Kerr-Newman and rotating regular black holes, *Phys. Rev. D* **97**, 064021 (2018).
- [49] P. V. P. Cunha and C. A. R. Herdeiro, Shadows and strong gravitational lensing: A brief review, *Gen. Relativ. Gravit.* **50**, 42 (2018).
- [50] C. Bambi and E. Barausse, Constraining the quadrupole moment of stellar-mass black-hole candidates with the continuum fitting method, *Astrophys. J.* **731**, 121 (2011).
- [51] K. Glampedakis and S. Babak, Mapping spacetimes with LISA: Inspiral of a test body in a quasi-Kerr field, *Classical Quantum Gravity* **23**, 4167 (2006).
- [52] J. B. Hartle, Slowly rotating relativistic stars. I. Equations of structure, *Astrophys. J.* **150**, 1005 (1967); J. B. Hartle and K. S. Thorne, Slowly rotating relativistic stars. II. Models for neutron stars and supermassive stars, *Astrophys. J.* **153**, 807 (1968).
- [53] C. Bambi and G. Lukes-Gerakopoulos, Testing the existence of regions of stable orbits at small radii around black hole candidates, *Phys. Rev. D* **87**, 083006 (2013).
- [54] C. Bambi, Evolution of the spin parameter of accreting compact objects with non-Kerr quadrupole moment, *J. Cosmol. Astropart. Phys.* **05** (2011) 009.
- [55] V. P. Frolov and I. D. Novikov, *Black Hole Physics: Basic Concepts and New Developments* (Kluwer Academic, Dordrecht and Boston, 1998).
- [56] X. Wu, T. Y. Huang, X. S. Wan, and H. Zhang, Comparison among correction methods of individual Kepler energies in n-body simulations, *Astron. J.* **133**, 2643 (2007).

- [57] D. Z. Ma, X. Wu, and J. F. Zhu, Velocity scaling method to correct individual Kepler energies, *New Astron.* **13**, 216 (2008); D. Z. Ma, X. Wu, and F. Y. Liu, Velocity corrections to kepler energy and laplace integral, *Int. J. Mod. Phys. C* **19**, 1411 (2008); D. Z. Ma, X. Wu, and S. Y. Zhong, Extending Nacozy's approach to correct all orbital elements for each of multiple bodies, *Astrophys. J.* **687**, 1294 (2008).
- [58] M. Z. Wang, S. B. Chen, and J. L. Jing, Chaos in the motion of a test scalar particle coupling to Einstein tensor in Schwarzschild-Melvin black hole spacetime, *Eur. Phys. J. C* **77**, 208 (2017).
- [59] R. Genzel, F. Eisenhauer, and S. Gillessen, The Galactic Center massive black hole and nuclear star cluster, *Rev. Mod. Phys.* **82**, 3121 (2010).